Spectroscopic Signature of the Superparamagnetic Transition and Surface Spin Disorder in CoFe$_2$O$_4$ Nanoparticles

Qi -C. Sun,[†] Christina S. Birkel,[‡,⊥] Jinbo Cao,[§] Wolfgang Tremel,[‡] and Janice L. Musfeldt[†,*]

[†]Department of Chemistry, University of Tennessee, Knoxville, Tennessee 37996, United States, [‡]Institut für Anorganische Chemie und Analytische Chemie der Johannes Gutenberg-Universität, Duesbergweg 10-14, D-55099 Mainz, Germany, and [§]Electronic Materials and Physics Laboratory, General Electric Global Research Center, One Research Circle, Niskayuna, New York 12309, United States. [⊥]Present address: Materials Research Laboratory, University of California, Santa Barbara, California 93106, United States.

Phonons are incisive probes of charge and bonding in extended solids. This exquisite sensitivity can be traced to the influence of charge on the shape of the potential surface.[1,2] When combined with vibrational property measurements, analysis of these interactions reveals Born effective charge, charge ordering and disproportionation, and proximity effects among others.[3−9] Systems in which the lattice is coupled with spin are less common and have received significantly less attention. When magnetoelastic interactions are present, investigations reveal local lattice distortions, coupling mechanisms, and new types of transitions that take place due to collective effects.[10−21] CoFe$_2$O$_4$ attracted our attention as a rich system with which to explore these developments because (i) coupling in a magnetic oxide is anticipated to be large[13−15] and (ii) confinement effects[21−24] can be explored.

CoFe$_2$O$_4$ crystallizes in an inverse spinel structure with the general formula AB$_2$O$_4$ where A and B denote tetrahedral and octahedral cation sites in a close-packed oxygen environment.[25,26] The unit cell is cubic (a = 0.8391 nm at 300 K) with 8 formula units and a $Fd\overline{3}m$ space group (Figure 1a).[25−27] Group theory predicts four triply degenerate (T_{1u}) infrared-active vibrational modes.[28] Several authors have analyzed the lattice dynamics of the AB$_2$O$_4$ system and compared their findings with infrared and Raman data. This work revealed mode assignments, displacement patterns, charge and bonding information, and thermodynamics.[27,28] Below the 860 K Curie temperature (T_C), CoFe$_2$O$_4$ presents

ABSTRACT
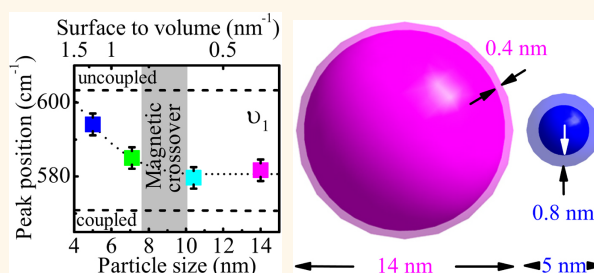
Phonons are exquisitely sensitive to finite length scale effects in a wide variety of materials. To investigate confinement in combination with strong magnetoelastic interactions, we measured the infrared vibrational properties of CoFe$_2$O$_4$ nanoparticles and compared our results to trends in the coercivity over the same size range and to the response of the bulk material. Remarkably, the spectroscopic response is sensitive to the size-induced crossover to the superparamagnetic state, which occurs between 7 and 10 nm. A spin−phonon coupling analysis supports the core−shell model. Moreover, it provides an estimate of the magnetically disordered shell thickness, which increases from 0.4 nm in the 14 nm particles to 0.8 nm in the 5 nm particles, demonstrating that the associated local lattice distortions take place on the length scale of the unit cell. These findings are important for understanding finite length scale effects in this and other magnetic oxides where magnetoelastic interactions are important.

long-range collinear ferrimagnetic order (with antiferromagnetic intersublattice exchange interactions). Local canting and anisotropy reduces the moment to 3.35 μ_B at 300 K, and the easy magnetization axis is along [100].[25] The discovery of nanoscale CoFe$_2$O$_4$ enables investigation of finite length scale effects. Major findings at this time include synthetic techniques that yield excellent size/shape control,[29−32] the crossover to single
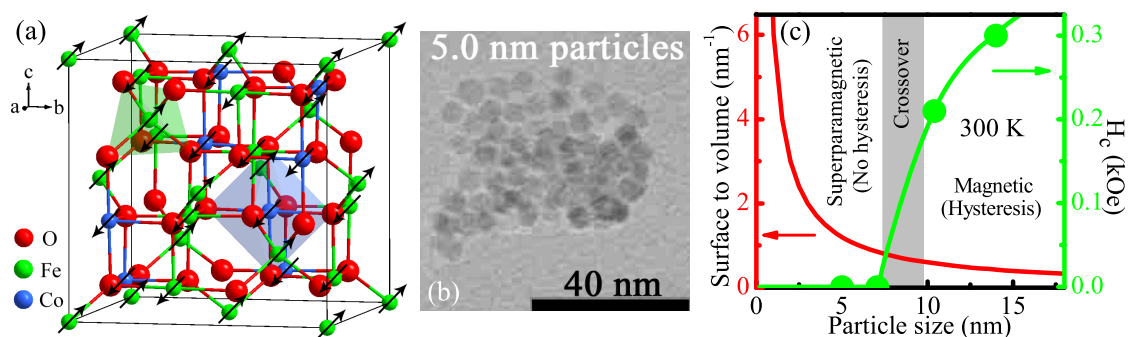
Figure 1. (a) 300 K crystal structure of $CoFe_2O_4$ spinel with ferrimagnetic ordering along the [100] direction.[25] (b) TEM image of the 5.0 nm particles. (c) Surface-to-volume ratio and coercivity as a function of particle diameter. The magnetic crossover regime (from the hysteretic ferrimagnetic regime at large sizes to the superparamagnetic state at small particle sizes) is denoted by the vertical gray band. The green line connecting coercivity data points guides the eye.

domain behavior at ~40 nm,[32] the cubic anisotropy,[33−35] and superparamagnetism in small particles.[30−36,37] As magnetic insulators,[26] spinels are attractive for device applications.[38−40]

In order to investigate finite length scale effects in $CoFe_2O_4$, we measured the infrared vibrational properties of a series of nanoparticles and compared the results to coercivity trends over the same size range and the response of the bulk material. Strong magnetoelastic coupling enables the spectra to convey magnetic property information that is hidden in many other systems. Magnetoelastic coupling is manifest as mode splitting of bulk $CoFe_2O_4$ (from which we extract a ~6.3 N/m spin−phonon coupling constant) and peak positions that change with size in the confined materials. A detailed analysis of spin−phonon coupling in the nanoparticles reveals a size-induced crossover to the superparamagnetic state between 10 and 7 nm that correlates with coercivity and surface area trends. At the same time, our coupling analysis provides spectral support for the core−shell model in which a core of aligned spins is surrounded by a magnetically disordered shell. Remarkably, the spectral data also allow a shell thickness analysis. We find a 0.4 nm shell thickness in the 14 nm particles and a 0.8 nm shell thickness in the 5 nm particles. These values are consistent with the 0.8391 nm unit cell size, and the trend is in excellent agreement with the neutron scattering data of Lin *et al.* (1.2 nm shell in 4 nm particles).[41] Taken together, these findings showcase the power and breadth of vibrational spectroscopy for fundamental property investigations of magnetic oxides.

RESULTS AND DISCUSSION

Superparamagnetic Transition in $CoFe_2O_4$ Nanoparticles. Figure 1c shows coercivity, H_c, as a function of nanoparticle size. The 14.0 and 10.4 nm particles display magnetic hysteresis loops and nonzero coercivities, whereas hysteresis loops are not observed in the 7.1 and 5.0 nm materials (Figure S3 and Table SI). There is clearly a size-driven crossover between the hysteretic

and nonhysteretic ($H_c = 0$) regimes in the 7−10 nm size range. Above the magnetic crossover, the 14.0 and 10.4 nm $CoFe_2O_4$ nanoparticles are in the ferrimagnetic state. We can understand the behavior of these larger particles by considering the magnetocrystalline anisotropy energy, E_A, which goes as $KV \sin^2\theta$.[36,42,43] Here, K is the magnetocrystalline anisotropy, V is the nanoparticle volume, and θ is the angle between the magnetization direction and the easy axis of the nanoparticle. A hysteresis loop is observed when magnetocrystalline anisotropy is larger than the thermal energy,[36,43] which in this case is 300 K. A reduced remanence can also be extracted (Supporting Information). Below the magnetic crossover, the 7.1 and 5.0 nm particles are in the superparamagnetic state.[32] Here, spin acts as a giant moment, the energy landscape is characterized by doubly degenerate minima separated by an energy barrier, and when temperature is larger than the barrier, the magnetization direction flips randomly.[38,44] Stoner−Wohlfarth theory provides a framework within which we can understand these effects.[37,42] Here, the coercivity of a single-domain particle is expressed as $2K/\mu_0 M_s$, where K is the previously mentioned magnetocrystalline anisotropy, M_s is the saturation magnetization, and μ_0 is the permeability of free space. In the superparamagnetic state, magnetocrystalline anisotropy is overcome by thermal effects, a situation that renders K unimportant (and effectively zero). Figure 1c also displays the surface-to-volume ratio as a function of particle size. The $H_c > 0$ behavior of the 14.0 and 10.4 nm $CoFe_2O_4$ particles correlates with low surface-to-volume ratios, whereas the superparamagnetic ($H_c = 0$) state of the 7.1 and 5.0 nm particles correlates with larger surface-to-volume ratios.[31,36,45] In the following discussion, we combine these magnetic property trends with complementary vibrational spectroscopies to more deeply investigate the ferrimagnetic → superparamagnetic transition and signatures of surface spin disorder in magnetic nanoparticles.

Spin−Phonon Coupling in Bulk $CoFe_2O_4$. Figure 2a displays the infrared absorption of bulk and nanoscale $CoFe_2O_4$. The spectrum of the bulk material shows three vibrational modes at ~577 (ν_1), 382 (ν_2), and
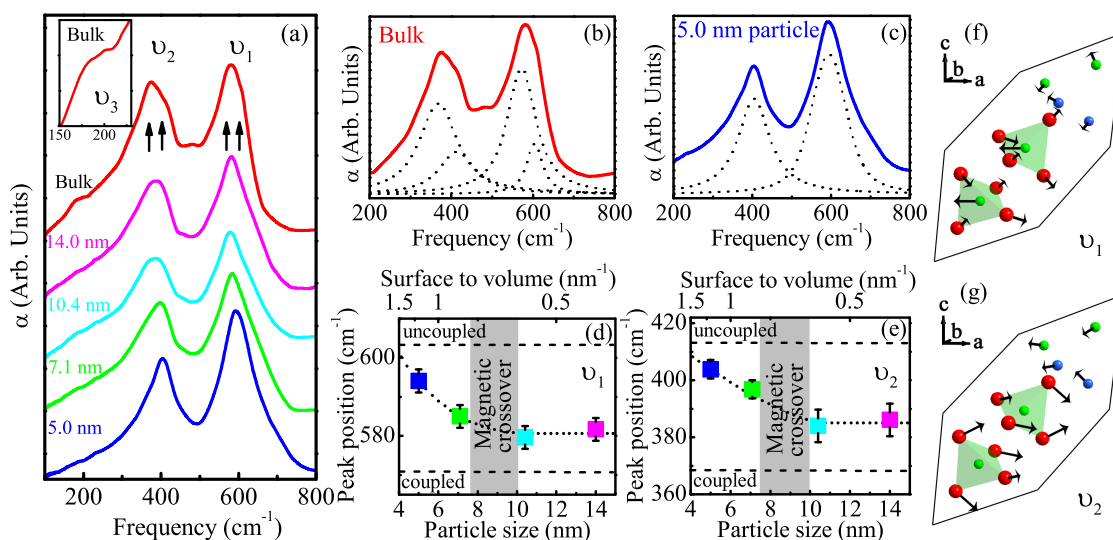
Figure 2. (a) 300 K absorption spectra of bulk powder and nanoscale $CoFe_2O_4$. The particle sizes are indicated, and the curves are vertically shifted for clarity. Inset: Close-up view of ν_3 in the bulk powder. (b) Example peak fit of the bulk $CoFe_2O_4$ spectrum using Voigt line shapes. Two oscillators are required to fit each mode. (c) Example peak fit of the 5.0 nm nanoparticle spectrum using Voigt line shapes. Only one oscillator is required to fit each mode. (d and e) Peak position of ν_1 and ν_2 as a function of particle size. The dashed lines indicate the limiting bulk values with and without spin−phonon coupling, and the dotted lines guide the eye.[21,46] The gray shaded area indicates the transition regime (from ferrimagnetic at large particle sizes to superparamagnetic at small sizes.) (f and g) Schematic view of calculated displacement patterns of ν_1 and ν_2 vibrational modes in $CoFe_2O_4$ in the rhombohedral primitive cell.[27,28,47] Here, the shaded green polyhedra denote tetrahedral sites, and the top four ions correspond to octahedral positions.

190 cm^{-1} (ν_3), in agreement with prior results.[27,48,49] In the nanoparticles, ν_3 is extremely weak, probably due to combined phonon lifetime effects, damping, and (for coupled systems such as $CoFe_2O_4$) magnetic relaxation time effects.[21,36,50−52] We therefore focus on trends in ν_1 and ν_2 to reveal the spectroscopic signatures of the superparamagnetic transition and surface spin disorder. Figure 2f and g display the calculated displacement patterns for ν_1 and ν_2.[27,53] For ν_1, the tetrahedral metal centers vibrate against the oxygen cage, and the octahedral metal centers vibrate against each other and the surrounding oxygen sites. For ν_2, the tetrahedral metal center is fixed and oxygen cage vibration is balanced by octahedral cation + cage motion. Here, the octahedral metal center vibrates against the other B site cation and the surrounding oxygen centers.

We can understand the peak shape in bulk $CoFe_2O_4$ by recalling that this system is ferrimagnetic at room temperature.[26] Figure 2b shows a representative two-oscillator fit to ν_1 and ν_2. The presence of magnetic ordering[26] motivates our assignment based upon strong spin−phonon coupling and provides a natural physical explanation for the observed doublet structure in this and other spinels.[21,27,46] The motion of ions in a solid is well known to couple with charge.[6,51,54,55] This type of interaction is the basis for traditional dynamics calculations that yield mode frequencies and displacement patterns of the sort discussed above. In some materials, the motion of ionic centers also couples with spins.[14,21,46] The Hamiltonian for the ion

motion is written as $\mathscr{H} = p^2/2\mu + V(u)$. Here, $V(u)$ is the effective potential, u is the displacement, p is the translational momentum, and μ is the reduced mass. When the atomic centers in a unit cell vibrate, the exchange interactions become a function of the displacement, and spin−spin interaction changes the effective phonon potential. This generic mechanism couples spin to the lattice as[10,14,20,46]

$$\omega^2 = \omega_0{}^2 + \lambda\langle S_i \cdot S_j \rangle \tag{1}$$

where $\omega = (k/\mu)^{1/2}$ is the perturbed mode frequency (in the presence of spin−spin interactions, k is the spring constant), ω_0 is the bare phonon frequency without spin−spin interactions, $\lambda = 1/\mu \cdot J''$ is the macroscopic spin−phonon coupling constant,[56] J is the magnetic exchange, J'' is the second derivative with respect to u, and $\langle S_i \cdot S_j \rangle$ is the nearest-neighbor spin−spin correlation function. Here, we employ a single J Hamiltonian, where the exchange interaction is negative (positive) for antiferromagnetic (ferromagnetic) interactions.[57] For a system with dominant antiferromagnetic interactions, $\langle S_i \cdot S_j \rangle$ will be negative. This model predicts that a triply degenerate vibrational mode in a two-sublattice ferrimagnetic cubic environment (as exists in a system like MnO) will split into two branches below T_C.[21,46,58,59]

Let us apply these ideas to bulk $CoFe_2O_4$. The presence of both coupled and uncoupled components is evidenced by the doublet character of ν_1 and ν_2 (Figure 2b). Even ν_3 displays weak splitting (inset

Figure 2a).[60] A symmetry analysis reveals the origin of the coupled and uncoupled branches and the resultant mode splitting. The displacement patterns of ν_1 and ν_2 (Figure 2f and g) both show that the tetrahedral A sites have either (i) the same or (ii) zero directional motion. As a consequence, no coupling emanates from the A sublattice in the AB_2O_4 spinel structure. In other words, this branch has no spin−spin correlations. In contrast, ions of the B sublattice (formed by the octahedral metal sites) vibrate against each other. This symmetry is consistent with spin−phonon coupling, and the branch is softened by spin−spin interactions. The intersublattice motion also involves out-of-phase vibration and likewise contributes to coupling. The horizontal dashed lines in Figure 2d and e denote the uncoupled and coupled components of the phonon at higher and lower frequency, respectively. The size of the splitting ($\Delta\omega_{\nu_1} = -32$ cm^{-1} and $\Delta\omega_{\nu_2} = -46$ cm^{-1}) is a measure of the perturbation and is related to the coupling constant for each mode.

Equation 1 provides a framework within which we can estimate the spin−phonon coupling constants of ν_1 and ν_2 for bulk $CoFe_2O_4$. We already have the frequency shift from our measured data,[61] but we still need to obtain the spin−spin correlation function.[62] Here, we employ an approximate method that was originally developed for Fe_3O_4.[58,63] It assumes an Ising Hamiltonian, nearest-neighbor interactions, and the two-sublattice ferrimagnetic model.[58,63] Under these assumptions, we can write $\langle S_i \cdot S_j \rangle = \Sigma S_{Bi} \cdot S_{Bj} - \Sigma S_{Ai} \cdot S_{Bj}$ for a single formula unit. Here, S_{Ai} denotes the spin at the A sublattice site, and S_{Bi} denotes the spin at the B sublattice site. Substituting $S = 5/2$ for Fe^{3+} and $S = 3/2$ for Co^{2+}, we find $\langle S_i \cdot S_j \rangle = -13/2$ for the fully inverted spinel.[56] $CoFe_2O_4$ is, however, known to display an inversion fraction of 0.75,[64] and the chemical formula is better written as $(Co_{0.25}^{2+}Fe_{0.75}^{3+})(Co_{0.75}^{2+}Fe_{1.25}^{3+})O_4$.[65] For the partially inverted case, we find $\langle S_i \cdot S_j \rangle = -9/8$.[56] With the latter value of the spin−spin correlation function and the previously mentioned frequency shifts,[61] we can roughly estimate the coupling constant of both modes as $J'' = \lambda\mu \approx 6.3$ N/m. In this calculation, we employed $\langle S_i \cdot S_j \rangle$ for the partially inverted spinel because it most closely resembles the situation in bulk $CoFe_2O_4$. The error bars are large (probably ± 1 or 2 N/m), mainly due to uncertainties in $\langle S_i \cdot S_j \rangle$. On the other hand, the extracted coupling constant of the partially inverse spinel ($J'' = \lambda\mu \approx 6.3$ N/m) is similar to the values found in other oxides such as MnO and $ZnCr_2O_4$.[13,14,21,66]

Spin−Phonon Coupling in $CoFe_2O_4$ Nanoparticles. We also employed standard peak-fitting techniques to reveal size-dependent trends in the position of ν_1 and ν_2.[67] The line shapes in the various nanoparticle samples are much more symmetric than that of the bulk due to the short phonon lifetime and fast magnetic relaxation time.[21,36,50−52,68,69] As a result, only one oscillator is needed to fit each mode (Figure 2c). Figure 2d and e

summarize the behavior of ν_1 and ν_2 as a function of nanoparticle size. The resonance frequencies increase with decreasing size through the magnetic crossover regime. This trend parallels the diverging surface-to-volume ratio (Figure 1c) and suggests a correlation with the transition to the superparamagnetic state and the development of surface spin disorder.[45] This connection is discussed below. As anticipated, the data points are positioned between the low- and high-frequency limits defined by coupled and uncoupled branches of each phonon in the bulk.

Spin−phonon coupling in the $CoFe_2O_4$ nanoparticles is different than in the bulk. This is because robust magnetic order exists primarily in the core, whereas the shell has a more random spin arrangement.[45] Magnetoelastic coupling is therefore different in the two regions. Interestingly, infrared spectroscopy is sensitive to this change. Although there is no splitting of ν_1 and ν_2 (Figure 2a), these features still carry information on the coupling in an average way that causes peak positions to shift with decreasing particle size. Of course, it is not really particle size that matters here but the relative proportion of core and shell. The core−shell model (where we assume that the particle consists of a core of aligned spins surrounded by a magnetically disordered shell)[45] accounts for these effects. We consider each region in turn and then bring them together.

In the core of a single-domain nanoparticle such as $CoFe_2O_4$,[32] spins align ferrimagnetically according to their various exchange interactions,[41,45] a process that mirrors the development of magnetic order in the bulk. Phonons that reside primarily in the core are sensitive to this magnetic structure, and they engage in spin−phonon coupling just like the bulk. Core phonon modes thus possess both coupled and uncoupled branches, as previously discussed, although confinement effects reduce the phonon lifetime[21,51,52,68] to yield only an averaged spectral response. This occurs because the phonon lifetime ($10^{-14}−10^{-13}$ s) is shorter than the spectroscopic time scale ($10^{-12}−10^{-13}$ s),[69] so the spectrum will measure multiple phonon vibrations in the same time period, which eliminates the possibility of distinguishing between coupled and uncoupled branches.[21,51,52,68]

The surface of a magnetic nanoparticle is different. Here, large surface strains, broken bonds, and broken exchange interactions between magnetic centers cause surface spins to lose their order.[41,45] Under these conditions, the spin−spin correlation function $\langle S_i \cdot S_j \rangle$ will be close to zero. Since $\omega^2 = \omega_0^2 + \lambda\langle S_i \cdot S_j \rangle$, the vibrational contribution of the nanoparticle shell will thus be a peak at the unperturbed phonon frequency, ω_0, regardless of the value of λ. In other words, there can be no coupling without spin order. Variable-temperature infrared spectroscopy provides an additional test for the presence of surface spin disorder.[41,45]

Our experiments on the 5 nm particles reveal a gradual red-shift of the peak positions with decreasing temperature (on the order of 5 cm^{-1} for ν_1 and 2 cm^{-1} for ν_2), consistent with presence of surface spin disorder at high temperature and the possibility of a low-temperature surface spin glass state.[41,45] These data are available in the Supporting Information.

Let us bring the behavior of the core and shell together. We already argued that the spectrum of the nanoparticles catches only the weighted average value of the coupled and uncoupled branches of each mode due to the short phonon lifetime and fast magnetic relaxation time.[21,36,50−52,68] This averaged response can be expressed as $\omega_{av} = x\omega_{shell} + (1 - x)\omega_{core}$. Here, ω_{av} is the weighted average frequency, x is the volume fraction of the shell, $(1 - x)$ is the volume fraction of the core, and ω_{core} and ω_{shell} are the core and shell phonon frequencies, respectively. Moreover, ω_{core} is always less than ω_{shell} because the core includes the coupled branch contribution whereas the shell does not. If we assume that ω_{core} and ω_{shell} do not change with size over the range of our investigation, larger values of x will shift the observed peak at ω_{av} to higher frequency. This is in agreement with the data in Figure 2d and e, and it provides a natural explanation for the similarity between these trends and the surface-to-volume ratio in Figure 1c. As shown in Figure 2d and e, the peak position of the 7.1 nm particles is elevated compared to that of the larger particles, and ω_{av} of the 5.0 nm particles is approaching the bare phonon frequency of the bulk. Moreover, both the 5 and 7 nm particles are in the superparamagnetic state under these conditions. The spectral sensitivity to the superparamagnetic transition in these ferrimagnetic spinel nanoparticles is thus due to magnetoelastic coupling (with a boundary at ~0.5($\omega_0 + \omega$) of bulk values estimated from Figure 2d and e). Moreover, the core−shell model captures the physics of this situation extremely well.

Using Vibrational Spectroscopy to Estimate Shell Thickness. We can also employ our spectral data to estimate the relative size of the core and shell. First, we calculate the weighted average phonon frequencies of ν_1 and ν_2 for the bulk material. This is done using peak-fitted mode positions and the normalized areas of the coupled and uncoupled components.[56] Using ν_2 as an example, the weighted average frequency can be written as $\omega_{av} = y\omega + (1 - y)\omega_0$. The factors of y (0.69) and $(1 - y)$ (0.31) are the normalized areas of the coupled ($\omega = 368$ cm^{-1}) and uncoupled ($\omega_0 = 413$ cm^{-1}) branches of ν_2 in the bulk (Figure 3a). We find $\omega_{av} = 382$ cm^{-1}. This number rigorously describes the bulk and reasonably approximates the nanoparticle core. We further fix the core phonon frequency in our set of 14, 10, 7, and 5 nm particles to be that of the bulk. In other words, we assume that this value ($\omega_{av} = 382$ cm^{-1}) does not depend on size. Lastly, we also allow the shell phonon to be represented by the uncoupled phonon in the
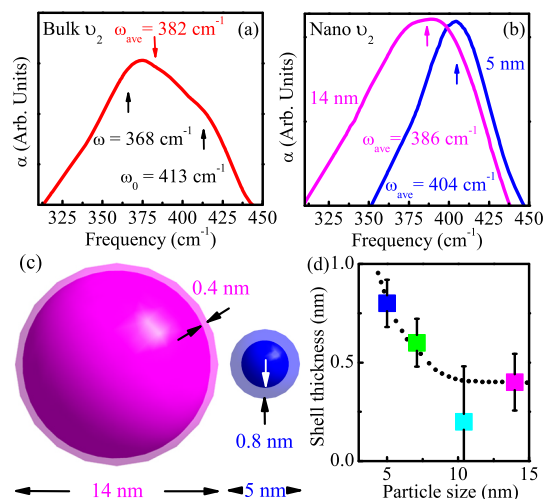

Figure 3. (a) Close-up view of the ν_2 vibrational mode of bulk CoFe$_2$O$_4$ where the perturbed (ω) and unperturbed (ω_0) frequencies are clearly resolved due to magnetoelastic coupling. The weighted average position of the coupled and uncoupled branches, ω_{av}, is also indicated. (b) Close-up view of ν_2 for the 14 and 5 nm particles where the spectral peak represents the weighted average of the coupled and uncoupled branches. In other words, ω and ω_0 are smeared together due to lifetime effects, and only ω_{av} is observed. (c) Schematic view of our findings from the core−shell model for the 14 and 5 nm particles, respectively. The extracted shell thicknesses of 0.4 and 0.8 nm are comparable with the 0.8391 nm unit cell size[26] for bulk CoFe$_2$O$_4$. (d) Shell thickness as a function of particle size determined by a spin−phonon coupling analysis. The dotted line guides the eye.

bulk, an assumption that is justified because $\langle S_i \cdot S_j \rangle \approx 0$. Using the weighted average phonon frequency of the 5 nm particles from the measured spectrum ($\omega_{av} = 404$ cm^{-1}, Figure 3b) and our expression for the overall average response $\omega_{av} = x\omega_{shell} + (1 - x)\omega_{core}$, we can back-calculate the volume fraction of the shell. We find $x = 0.71$ for the 5 nm particles. An analysis of ν_1 yields a similar value ($x = 0.63$). Using the average of these two quantities ($x = 0.67$), we can estimate the shell thickness as $x = (4/3\pi R^3 - 4/3\pi r^3)/(4/3\pi R^3)$. Here, R is the nanoparticle radius, and r is the radius of the core. We find $r = 1.7$ nm for the 5 nm particles. The shell thickness is therefore $2.5 - 1.7 = 0.8$ nm. A similar analysis of the 14 nm particles yields an 0.4 nm shell thickness. The extracted shell thicknesses of 0.4 and 0.8 nm for the 14 and 5 nm particles are comparable with the 0.8391 nm unit cell size for bulk CoFe$_2$O$_4$.[26] We therefore conclude that the surface distortion takes place within the outermost unit cell, a finding that is consistent with other length scale estimates of spin disorder.[45,70−72]

Figure 3c displays a schematic view of the 14 and 5 nm CoFe$_2$O$_4$ particles within the core−shell picture. Shell thickness is clearly not a constant. Instead, it increases from 0.4 to 0.8 nm over the range of our investigation. We can see this result more clearly in Figure 3d. While the 1.2 nm shell thickness in the 4 nm particles investigated by Lin *et al.*[41] is not strictly comparable with our data because the particles were

prepared by mechanical agitation rather than the synthetic techniques employed here,[29,30] the trend is strikingly preserved. In any case, the inverse relationship between shell thickness and particle size emanates from the large surface strains that introduce broken bonds (and interrupted exchange interactions between magnetic centers) in the small nanoparticles. We conclude that the large proportion of surface spin disorder in the small $CoFe_2O_4$ particles is responsible for the crossover to the superparamagnetic state.

CONCLUSIONS

To summarize, we measured the infrared vibrational properties of several different $CoFe_2O_4$ nanoparticles and compared the results to trends in the coercivity and to the spectrum of the bulk material. A detailed analysis of the magnetoelastic coupling allows us to extract a spin−phonon coupling constant of ∼6.3 N/m for the bulk. Moreover, we show that these same processes are sensitive to the size-dependent crossover in magnetic properties (in which the nanoparticles become superparamagnetic between 7 and 10 nm). In other words, magnetoelastic coupling in the confined system makes the mode position sensitive to the superparamagnetic transition. Combining this mode information with a spin−phonon coupling analysis reveals the applicability of the core−shell model with a core of aligned spins surrounded by a magnetically disordered shell. We use this model to evaluate the shell thickness and find that it is on the order of 1 unit cell. It increases from 0.4 nm in our 14 nm particles to 0.8 nm in the 5 nm particles. These findings are unique in that they verify the core−shell model from the spectroscopic point of view.

MATERIALS AND METHODS

Our $CoFe_2O_4$ particles were prepared by high-temperature decomposition of the metal precursors following the method of Sun *et al.*[29,30] Nearly monodisperse $CoFe_2O_4$ particles were obtained by varying the reaction time or the surfactant concentration. Four different particle sizes between 5 and 14 nm were prepared for this work. The synthetic details and characterization can be found in the Supporting Information. Figure 1b displays the transmission electron microscopy (TEM) image of the 5.0 nm diameter particles. The particles have a well-defined sphere-like shape. X-ray analysis indicates that the nanoparticles are essentially isostructural with the bulk (Figure S1). The preparation of pure $CoFe_2O_4$ nanoparticles is also confirmed by energy dispersive X-ray spectroscopy. The magnetic hysteresis loops for pressed powder samples were measured by a superconducting quantum interference device, and coercivity was extracted from the loop width (Figure S3). All of the $CoFe_2O_4$ nanoparticles of interest here are single-domain.[32] For comparison, bulk $CoFe_2O_4$ powder (99.31%) was purchased directly from Alfa Aesar.[73,74] Here, the crystallites are 0.1 mm diameter on average. For our spectroscopic work, the bulk powder and nanoparticles were mixed with paraffin (∼3 mass percent) to form isotropic composites. Transmittance was measured using a Bruker 113 V Fourier transform infrared spectrometer (20−5000 cm^{-1}; 0.5 cm^{-1} resolution) at room temperature. A helium-cooled bolometer detector was employed for added sensitivity. The absorption coefficient was obtained as $\alpha(\omega) = -(1/hd)\ln T(\omega)$, where h is the loading, d is the thickness, and $T(\omega)$ is the measured transmittance. Low-temperature experiments were carried out with an open flow cryostat. Traditional peak fitting techniques were employed as appropriate.

Conflict of Interest: The authors declare no competing financial interest.

Supporting Information Available: The synthesis, characterization, low-temperature infrared behavior, and detailed calculation of the spin−spin interaction are available free of charge *via* the Internet at http://pubs.acs.org.

REFERENCES AND NOTES

1. Lee, C. Y.; Gonze, X. Lattice Dynamics and Dielectric Properties of SiO_2 Stishovite. *Phys. Rev. Lett.* **1994**, *72*, 1686–1689.
2. Savrasov, S. Y.; Kotliar, G. Linear Response Calculations of Lattice Dynamics in Strongly Correlated Systems. *Phys. Rev. Lett.* **2003**, *90*, 056401.
3. Lucovsky, G.; Martin, R. M.; Burstein, E. Localized Effective Charges in Diatomic Crystals. *Phys. Rev. B* **1971**, *4*, 1367–1374.
4. Musfeldt, J. L.; Kamaras, K.; Tanner, D. B. Infrared Studies of the Phase Transition in the Organic Charge-Transfer Salt N-Propylquinolinium Ditetracyanoquinodimethane. *Phys. Rev. B* **1992**, *45*, 10197–10205.
5. Resta, R.; Posternak, M.; Baldereschi, A. Towards a Quantum Theory of Polarization in Ferroelectrics: The Case of $KNbO_3$. *Phys. Rev. Lett.* **1993**, *70*, 1010–1013.
6. Homes, C. C.; Vogt, T.; Shapiro, S. M.; Wakimoto, S.; Ramirez, A. P. Optical Response of High-Dielectric-Constant Perovskite-Related Oxide. *Science* **2001**, *293*, 673–676.
7. Yamamoto, T.; Uruichi, M.; Yamamoto, K.; Yakushi, K.; Kawamoto, A.; Taniguchi, H. Examination of the Charge-Sensitive Vibrational Modes in Bis(ethylenedithio)tetrathiafulvalene. *J. Phys. Chem. B* **2005**, *109*, 15226–15235.
8. Kim, M.; Barath, H.; Cooper, S. L.; Abbamonte, P.; Fradkin, E.; Ruebhausen, M.; Zhang, C. L.; Cheong, S. W. Raman Scattering Studies of the Temperature- and Field-Induced Melting of Charge Order in $La_xPr_yCa_{1-x-y}MnO_3$. *Phys. Rev. B* **2008**, *77*, 134411.
9. Xu, X. S.; de Groot, J.; Sun, Q. C.; Sales, B. C.; Mandrus, D.; Angst, M.; Litvinchuk, A. P.; Musfeldt, J. L. Lattice Dynamical Probe of Charge Order and Antipolar Bilayer Stacking in $LuFe_2O_4$. *Phys. Rev. B* **2010**, *82*, 014304.
10. Lockwood, D. J.; Cottam, M. G. The Spin-Phonon Interaction in FeF_2 and MnF_2 Studied by Raman Spectroscopy. *J. Appl. Phys.* **1988**, *64*, 5876–5878.
11. Hase, M.; Terasaki, I.; Uchinokura, K. Observation of the Spin-Peierls Transition in Linear Cu^{2+} (Spin-1/2) Chains in an Inorganic Compound $CuGeO_3$. *Phys. Rev. Lett.* **1993**, *70*, 3651–3654.
12. Gasparov, L. V.; Tanner, D. B.; Romero, D. B.; Berger, H.; Margaritondo, G.; Forro, L. Infrared and Raman Studies of

the Verwey Transition in Magnetite. *Phys. Rev. B* **2000**, *62*, 7939–7944.

13. Sushkov, A. B.; Tchernyshyov, O.; Ratcliff, W.; Cheong, S. W.; Drew, H. D. Probing Spin Correlations with Phonons in the Strongly Frustrated Magnet $ZnCr_2O_4$. *Phys. Rev. Lett.* **2005**, *94*, 137202.

14. Fennie, C. J.; Rabe, K. M. Magnetically Induced Phonon Anisotropy in $ZnCr_2O_4$ from First Principles. *Phys. Rev. Lett.* **2006**, *96*, 205505.

15. Aguilar, R. V.; Sushkov, A. B.; Choi, Y. J.; Cheong, S. W.; Drew, H. D. Spin-Phonon Coupling in Frustrated Magnet $CdCr_2O_4$. *Phys. Rev. B* **2008**, *77*, 092412.

16. Lee, S.; Pirogov, A.; Kang, M.; Jang, K.-H.; Yonemura, M.; Kamiyama, T.; Cheong, S. W.; Gozzo, F.; Shin, N.; Kimura, H.; et al. Giant Magneto-Elastic Coupling in Multiferroic Hexagonal Manganites. *Nature* **2008**, *451*, 805–808.

17. Vergara, L. I.; Cao, J.; Rogado, N.; Wang, Y. Q.; Chaudhury, R. P.; Cava, R. J.; Lorenz, B.; Musfeldt, J. L. Magnetoelastic Coupling in Multiferroic $Ni_3V_2O_8$. *Phys. Rev. B* **2009**, *80*, 052303.

18. Kim, M.; Chen, X. M.; Joe, Y. I.; Fradkin, E.; Abbamonte, P.; Cooper, S. L. Mapping the Magnetostructural Quantum Phases of Mn_3O_4. *Phys. Rev. Lett.* **2010**, *104*, 136402.

19. Schleck, R.; Moreira, R. L.; Sakata, H.; Lobo, R. Infrared Reflectivity of the Phonon Spectra in Multiferroic $TbMnO_3$. *Phys. Rev. B* **2010**, *82*, 144309.

20. Lee, J. H.; Fang, L.; Vlahos, E.; Ke, X. L.; Jung, Y. W.; Kourkoutis, L. F.; Kim, J. W.; Ryan, P. J.; Heeg, T.; Roeckerath, M.; et al. A Strong Ferroelectric Ferromagnet Created by Means of Spin-Lattice Coupling. *Nature* **2010**, *466*, 954–958.

21. Sun, Q. C.; Baker, S. N.; Christianson, A. D.; Musfeldt, J. L. Magnetoelastic Coupling in Bulk and Nanoscale MnO. *Phys. Rev. B* **2011**, *84*, 014301.

22. Song, R.-Q.; Xu, A.-W.; Yu, S.-H. Layered Copper Metagermanate Nanobelts: Hydrothermal Synthesis, Structure, and Magnetic Properties. *J. Am. Chem. Soc.* **2007**, *129*, 4152–4153.

23. Nakhjavan, B.; Tahir, M. N.; Panthoefer, M.; Gao, H.; Schladt, T. D.; Gasi, T.; Ksenofontov, V.; Branscheid, R.; Weber, S.; Kolb, U.; et al. Synthesis, Characterization and Functionalization of Nearly Mono-Disperse Copper Ferrite Cu_x-$Fe_{3-x}O_4$ Nanoparticles. *J. Mater. Chem.* **2011**, *21*, 6909–6915.

24. Masala, O.; Seshadri, R. Spinel Ferrite/MnO Core/Shell Nanoparticles: Chemical Synthesis of All-Oxide Exchange Biased Architectures. *J. Am. Chem. Soc.* **2005**, *127*, 9354–9355.

25. Teillet, J.; Bouree, F.; Krishnan, R. Magnetic Structure of $CoFe_2O_4$. *J. Magn. Magn. Mater.* **1993**, *123*, 93–96.

26. Kim, S. J.; Lee, S. W.; An, S. Y.; Kim, C. S. Mössbauer Studies of Superexchange Interactions and Atomic Migration in $CoFe_2O_4$. *J. Magn. Magn. Mater.* **2000**, *215*, 210–212.

27. Waldron, R. D. Infrared Spectra of Ferrites. *Phys. Rev.* **1955**, *99*, 1727–1735.

28. Himmrich, J.; Lutz, H. D. Normal Coordinate Analyses and Lattice Dynamical Calculations of Spinel-Type $ZnCr_2O_4$. *Solid State Commun.* **1991**, *79*, 447–452.

29. Sun, S. H.; Zeng, H. Size-Controlled Synthesis of Magnetite Nanoparticles. *J. Am. Chem. Soc.* **2002**, *124*, 8204–8205.

30. Sun, S. H.; Zeng, H.; Robinson, D. B.; Raoux, S.; Rice, P. M.; Wang, S. X.; Li, G. X. Monodisperse MFe_2O_4 (M = Fe, Co, Mn) Nanoparticles. *J. Am. Chem. Soc.* **2004**, *126*, 273–279.

31. Bao, N. Z.; Shen, L. M.; Wang, Y. H. A.; Ma, J. X.; Mazumdar, D.; Gupta, A. Controlled Growth of Monodisperse Self-Supported Superparamagnetic Nanostructures of Spherical and Rod-Like $CoFe_2O_4$ Nanocrystals. *J. Am. Chem. Soc.* **2009**, *131*, 12900–12901.

32. Chinnasamy, C. N.; Jeyadevan, B.; Shinoda, K.; Tohji, K.; Djayaprawira, D. J.; Takahashi, M.; Joseyphus, R. J.; Narayanasamy, A. Unusually High Coercivity and Critical Single-Domain Size of Nearly Monodispersed $CoFe_2O_4$ Nanoparticles. *Appl. Phys. Lett.* **2003**, *83*, 2862–2864.

33. Laureti, S.; Varvaro, G.; Testa, A. M.; Fiorani, D.; Agostinelli, E.; Piccaluga, G.; Musinu, A.; Ardu, A.; Peddis, D. Magnetic

34. Rondinone, A. J.; Samia, A. C. S.; Zhang, Z. J. Superparamagnetic Relaxation and Magnetic Anisotropy Energy Distribution in $CoFe_2O_4$ Spinel Ferrite Nanocrystallites. *J. Phys. Chem. B* **1999**, *103*, 6876–6880.

35. Garcia-Otero, J.; Porto, M.; Rivas, J.; Bunde, A. Influence of the Cubic Anisotropy Constants on the Hysteresis Loops of Single-Domain Particles: A Monte Carlo Study. *J. Appl. Phys.* **1999**, *85*, 2287–2292.

36. Liu, C.; Zou, B. S.; Rondinone, A. J.; Zhang, J. Chemical Control of Superparamagnetic Properties of Magnesium and Cobalt Spinel Ferrite Nanoparticles Through Atomic Level Magnetic Couplings. *J. Am. Chem. Soc.* **2000**, *122*, 6263–6267.

37. Chen, Q.; Zhang, Z. J. Size-Dependent Superparamagnetic Properties of $MgFe_2O_4$ Spinel Ferrite Nanocrystallites. *Appl. Phys. Lett.* **1998**, *73*, 3156–3158.

38. Skomski, R. Nanomagnetics. *J. Phys.: Condens. Matter* **2003**, *15*, R841–R896.

39. Ma, J. X.; Mazumdar, D.; Kim, G.; Sato, H.; Bao, N. Z.; Gupta, A. A Robust Approach for the Growth of Epitaxial Spinel Ferrite Films. *J. Appl. Phys.* **2010**, *108*, 063917.

40. Shukoor, M. I.; Natalio, F.; Metz, N.; Glube, N.; Tahir, M. N.; Therese, H. A.; Ksenofontov, V.; Theato, P.; Langguth, P.; Boissel, J.-P.; et al. dsRNA-Functionalized Multifunctional Gamma-Fe_2O_3 Nanocrystals: A Tool for Targeting Cell Surface Receptors. *Angew. Chem., Int. Ed.* **2008**, *47*, 4748–4752.

41. Lin, D.; Nunes, A. C.; Majkrzak, C. F.; Berkowitz, A. E. Polarized Neutron Study of the Magnetization Density Distribution within a $CoFe_2O_4$ Colloidal Particle II. *J. Magn. Magn. Mater.* **1995**, *145*, 343–348.

42. Stoner, E. C.; Wohlfarth, E. P. A Mechanism of Magnetic Hysteresis in Heterogeneous Alloys. *Philos. Trans. R. Soc. A* **1948**, *240*, 599–642.

43. This expression could also make use of averaged values as in Sun, S. H.; Murray, C. B.; Weller, D.; Folks, L.; Moser, A. Monodisperse FePt Nanoparticles and Ferromagnetic FePt Nanocrystal Superlattices. *Science* **2000**, *287*, 1989–1992.

44. Gubin, S. P. *Magnetic Nanoparticles*; Wiley-VCH: Weinheim, 2009.

45. Kodama, R. H.; Berkowitz, A. E.; McNiff, E. J.; Foner, S. Surface Spin Disorder in $NiFe_2O_4$ Nanoparticles. *Phys. Rev. Lett.* **1996**, *77*, 394–397.

46. Luo, W. D.; Zhang, P. H.; Cohen, M. L. Splitting of the Zone-Center Phonon in MnO and NiO. *Solid State Commun.* **2007**, *142*, 504–508.

47. There are four Fe cations, two Ni cations, and eight O anions in the primitive unit cell.

48. Mitsuishi, A.; Yoshinaga, H.; Fujita, S. The Far Infrared Absorption of Ferrites. *J. Phys. Soc. Jpn.* **1958**, *13*, 1236–1237.

49. No v_4 absorption band[28] is observed, in line with Waldron's dynamics calculations[27] and the experimental work of Mitsuishi et al.[48]

50. Tung, L. D.; Kolesnichenko, V.; Caruntu, D.; Chou, N. H.; O'Connor, C. J.; Spinu, L. Magnetic Properties of Ultrafine Cobalt Ferrite Particles. *J. Appl. Phys.* **2003**, *93*, 7486–7488.

51. Wooten, F. *Optical Properties of Solids*; Academic Press: New York, 1972.

52. Fu, X. G.; An, H. Z.; Du, W. M. Temperature-Dependent Raman Scattering Studies in ZnSe Nanoparticles. *Mater. Lett.* **2005**, *59*, 1484–1490.

53. These calculations are based on the rhombohedral primitive unit cell[47] and are identical to results based on the standard unit cell.[28]

54. Sun, Q. C.; Xu, X. S.; Vergara, L. I.; Rosentsveig, R.; Musfeldt, J. L. Dynamical Charge and Structural Strain in Inorganic Fullerenelike MoS_2 Nanoparticles. *Phys. Rev. B* **2009**, *79*, 205405.

55. Sun, Q. C.; Xu, X. S.; Baker, S. N.; Christianson, A. D.; Musfeldt, J. L. Experimental Determination of Ionicity in MnO Nanoparticles. *Chem. Mater.* **2011**, *23*, 2956–2960.

56. Additional detail is given in the Supporting Information for the synthesis, characterization, low-temperature behavior, and detailed calculation.

57. For a ferrimagnet, we usually consider a two-sublattice model with spin operators S_{Ai} at the sublattice A site (tetrahedral) and spin operators S_{Bi} at the sublattice B site (octahedral). The Hamiltonian of the system is $\mathscr{H}_S = J_{A-A}\Sigma_{\langle ij\rangle_A}S_{Ai}\cdot S_{Aj} + J_{B-B}\Sigma_{\langle ij\rangle_B}S_{Bi}\cdot S_{Bj} + \Sigma_{\langle ij\rangle}S_{Ai}\cdot S_{Bj}$,[58] where the sums are over all sites of a three-dimensional cubic lattice. $\langle ij\rangle$ denotes the sum over the nearest neighbors, $\langle ij\rangle_A$ denotes the sum over the sites of A sublattice, and $\langle ij\rangle_B$ denotes the sum over the sties of B sublattice. The first two terms describe the ferromagnetic Heisenberg intrasublattice exchange, with exchange $J_{A-A} > 0$ and $J_{B-B} > 0$. The third term describes the intersublattice exchange, which is antiferromagnetic ($J_{A-B} < 0$).[58]

58. Karchev, N. Towards the Theory of Ferrimagnetism. *J. Phys.: Condens. Matter* **2008**, *20*, 325219.

59. For MnO, the doubly degenerate branch is in-plane and has no spin–spin correlations, whereas the singly degenerate component is in the [111] direction and is softened by spin–spin interactions.

60. Similar effects are observed in other magnetic oxides.[13,21]

61. For ν_1, $\omega = 2\pi \times 571$ cm^{-1} = 1.08×10^{14} Hz, and $\omega_0 = 2\pi \times 604$ cm^{-1} = 1.14×10^{14} Hz; For ν_2, $\omega = 2\pi \times 368$ cm^{-1} = 6.93×10^{13} Hz, and $\omega_0 = 2\pi \times 413$ cm^{-1} = 7.78×10^{13} Hz. Then $\omega^2 - \omega_0^2 \approx -1.3 \times 10^{27}$ Hz^2.

62. $\langle S_i \cdot S_j\rangle$ from inelastic neutron scattering is unfortunately not available, and a full accounting of the interactions in CoFe$_2$O$_4$ is rather daunting.

63. Mazo-Zuluaga, J.; Restrepo, J.; Munoz, F.; Mejia-Lopez, J. Surface Anisotropy, Hysteretic, and Magnetic Properties of Magnetite Nanoparticles: A Simulation Study. *J. Appl. Phys.* **2009**, *105*, 123907.

64. Ferreira, T. A. S.; Waerenborgh, J. C.; Mendonca, M.; Nunes, M. R.; Costa, F. M. Structural and Morphological Characterization of FeCo$_2$O$_4$ and CoFe$_2$O$_4$ Spinels Prepared by a Coprecipitation Method. *Solid State Sci.* **2003**, *5*, 383–392.

65. The transition metals do not change their oxidation states as they occupy different sites. See, for example, ref 34.

66. A simultaneous lattice distortion plays an important role in entangling the spin and lattice channels in these materials. MnO undergoes a cubic-to-rhombohedral structural transition at the 118 K Néel temperature (T_N),[21] and ZnCr$_2$O$_4$ displays a cubic-to-tetragonal structural transition at T_N.[14]

67. Cao, J.; Choi, J.; Musfeldt, J. L.; Lutta, S.; Whittingham, M. S. Effect of Sheet Distance on the Optical Properties of Vanadate Nanotubes. *Chem. Mater.* **2004**, *16*, 731–736.

68. Usually, we can estimate the phonon lifetime according to the full width at half-maximum (Γ) in the dielectric response $\varepsilon_2(\omega)$ as $\tau = \hbar/\Gamma$.[51] However, absorption is not directly related to dielectric constant $\varepsilon_2(\omega)$, so we cannot estimate lifetime only according to the absorption $\alpha(\omega)$. But as we know, the nanoparticles usually have much shorter phonon lifetime than the parent compound.[21,52] As the phonon lifetime is shorter than the spectroscopic time scale of the far-infrared ($<10^{-11}$ s),[69] the spectra measure only the average value for nanoparticles. Phonon lifetime effects thus prevent the observation of phonon splitting in the nanoparticles. In addition, we also need to consider the relaxation time (t) in the nanoparticles, $t = t_0 \exp(KV/k_BT)$,[36,50] where t_0 is on the order of 10^{-9}–10^{-13} s, k_B is Boltzmann's constant, T is the temperature, K is the anisotropy constant of the particle, and V is the volume of the particle. As 5 and 7 nm particles are in a superparamagnetic state, K can be considered as zero.[37] The relaxation time will be on the order of t_0, which is probably shorter than the spectroscopic time scale of the far-infrared ($<10^{-11}$ s).[69] The magnetization vector probably changes quickly between different states, but the spins are still bundled in the core of nanoparticles.[45] Spectroscopy experiments reveal average values of the two types of (split) phonons for both modes ν_1 and ν_2, which are different from the bulk.

69. Ito, T.; Hamaguchi, T.; Nagino, H.; Yamaguchi, T.; Kido, H.; Zavarine, I. S.; Richmond, T.; Washington, J.; Kubiak, C. P. Electron Transfer on the Infrared Vibrational Time Scale in the Mixed Valence State of 1,4-Pyrazine- and 4,4′-Bipyridine-Bridged Ruthenium Cluster Complexes. *J. Am. Chem. Soc.* **1999**, *121*, 4625–4632.

70. Peddis, D.; Cannas, C.; Piccaluga, G.; Agostinelli, E.; Fiorani, D. Spin-Glass-Like Freezing and Enhanced Magnetization in Ultra-Small CoFe$_2$O$_4$ Nanoparticles. *Nanotechnology* **2010**, *21*, 125705.

71. Didukh, P.; Greneche, J. M.; Slawska-Waniewska, A.; Fannin, P. C.; Casas, U. Surface Effects in CoFe$_2$O$_4$ Magnetic Fluids Studied by Mössbauer Spectrometry. *J. Magn. Magn. Mater.* **2002**, *242*, 613–616.

72. Peddis, D.; Yaacoub, N.; Ferretti, M.; Martinelli, A.; Piccaluga, G.; Musinu, A.; Cannas, C.; Navarra, G.; Greneche, J. M.; Fiorani, D. Cationic Distribution and Spin Canting in CoFe$_2$O$_4$ Nanoparticles. *J. Phys.: Condens. Matter* **2011**, *23*, 426004.

73. Serna, C. J.; Ocana, M.; Iglesias, J. E. Optical Properties of α-Fe$_2$O$_3$ Microcrystals in the Infrared. *J. Phys. C: Solid State Phys.* **1987**, *20*, 473–484.

74. CoFe$_2$O$_4$ bulk powder (99.31%) may still contain small amounts of iron oxide. According to the absorption of Fe$_2$O$_3$,[73] there is a strong absorption band at ∼330 cm^{-1}, but our spectrum is flat at this range. That means any impurity concentration is very small, and the effect of Fe$_2$O$_3$ can be ignored in our analysis. Our result is also very similar to Waldron's.[27]